Research Article | Vol. 28, No. 5 / 2 March 2020 / Optics Express 6320
Optics EXPRESS

Data processing and performance evaluation of a tempo-spatially mixed modulation imaging Fourier transform spectrometer based on stepped micro-mirror

BAIXUAN ZHAO,[1,2] JINGUANG LV,[1,4] JUN REN,[1,2] YUXIN QIN,[1] JIN TAO,[1] JINGQIU LIANG,[1,3] AND WEIBIAO WANG[1]

[1]State Key Laboratory of Applied Optics, Changchun Institute of Optics, Fine Mechanics and Physics, Chinese Academy of Sciences, Changchun, Jilin 130033, China
[2]University of Chinese Academy of Science, Beijing 100049, China
[3]liangjq@ciomp.ac.cn
[4]jinguanglv@163.com

Abstract: A novel tempo-spatially mixed modulation imaging Fourier transform spectrometer based on a stepped micro-mirror has the advantages of high throughput, compactness, and stability. In this paper, we present a method of image- and spectrum-processing and performance evaluation, which is utilized to obtain a high-quality reconstructed image without stitching gaps and a reconstructed spectrum with significantly reduced noise and side-lobe oscillation. A theoretical model of instrument line shape and signal-to-noise ratio is established to verify the effectiveness of non-uniformity sampling correction and spectral resolution enhancement. Meanwhile, the performance of the instrument was evaluated combined with experimental results.

1. Introduction

As a safe, real-time, and accurate monitoring technology, the imaging Fourier transform spectrometer (IFTS) can obtain two-dimensional image information and one-dimensional spectral information simultaneously. The image can guide the spatial position of the target while the spectra can analyze the composition and content of the target. Moreover, IFTS features high spectral resolution, high throughput, and high stability, with strong targeting, high sensitivity, high adaptability, and a longer working life [1].

According to different optical path difference (OPD) acquisition methods, IFTS is divided into three types: temporal modulation (TMIFTS), spatial modulation (SMIFTS), and tempo-spatially mixed modulation (TSMIFTS) [2]. TSMIFTS obtains the OPD in the spatial dimension and completes OPD accumulation in the time dimension. The interference system of TSMIFTS has no movable parts and slits. Therefore, TSMIFTS possesses high stability of SMIFTS and a high luminous flux of TMIFTS simultaneously.

TSMIFTS, due to the above characteristics, has garnered much interest, and currently has a variety of structures: Sagnac based [3], corner based [4], scanning-mirror based [5], and snapshot [6,7], popularized in many different fields. In TSMIFTS interference data processing, in 2010, Jian *et al.* researched the data processing process of a tempo-spatially mixed modulated polarization interference imaging spectrometer, which was modulated by polarized interference optoelectronic devices [8–11], and proposed a multi-spectral data reconstruction method [12,13]. In 2014, Kleinert *et al.* proposed a nonlinear spectral radiation calibration method to improve the accuracy of radiation measurement [14]. In 2017, Ferrec *et al.* used multiplicative decomposition to remove fringes from the interferogram [15]. In 2018, Yan *et al.* proposed a method of high spectral resolution channeled imaging spectropolarimetry based on a high-throughput tempo-spatially

#383401 https://doi.org/10.1364/OE.383401
Journal © 2020 Received 15 Nov 2019; revised 14 Jan 2020; accepted 26 Jan 2020; published 19 Feb 2020

Optics EXPRESS

mixed modulated mode Savart interferometer, greatly increasing the reconstructed-spectrum resolution [16,17].

In 2014, we presented a TSMIFTS that used a stepped micro-mirror, instead of a high-precision moving mirror to obtain the OPD, greatly improving stability and ensuring high throughput and certain spectral resolution [18]. We also performed a laboratory imaging experiment; however, due to the new structure of the interference core that introduced the stepped micro-mirror, data processing and performance evaluation of the instrument was not completed and had many problems. For example, the uneven width and edge distribution of the sub-steps of the micro-mirror caused stitching gaps of the reconstructed images, and the uneven height distribution of the sub-steps of the micro-mirror caused wavenumber shifts of the reconstructed spectra. The existing methods [12–17] provide a reference value, but cannot solve the inherent problems of this instrument. In this paper, we propose a TSMIFTS based on a stepped micro-mirror with a greater number of steps to achieve higher spectral resolution. Problems related to data processing are considered and corresponding solutions are proposed. Moreover, for potential applications, we evaluate instrument-performance indicators and propose methods to move indicators close to their theoretical values.

2. Instrument structure and parameters

2.1. Structure and working principle

Figure 1(a) shows that the stepped micro-mirror TSMIFTS comprises a scanning mirror, a first imaging system, a plane mirror, a beam splitter, a compensator plate, a stepped micro-mirror, a second imaging system, and a detector with a cold stop.

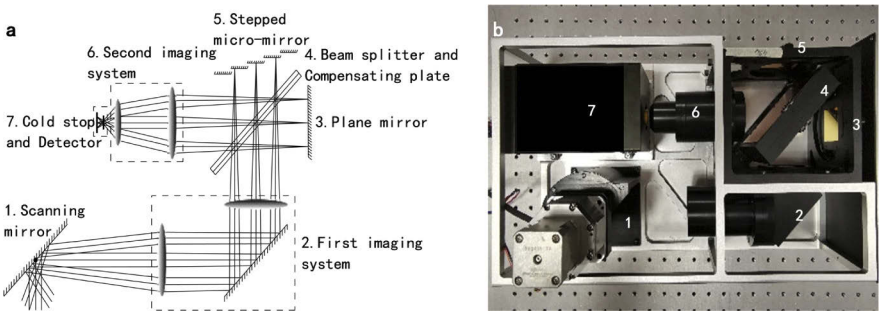

Fig. 1. (a) Simplified configuration of the TSMIFTS based on 128-step micro-mirror. (b) Internal structure of the prototype.

The working principle of the system is that at a certain time the light emitted by the target object passes through the scanning mirror and first imaging system, forming two primary image points on the plane mirror and the stepped micro-mirror, respectively. The two primary image points are ultimately imaged through the second imaging system on the focal plane of the detector, after being reflected by the plane mirror and micro-mirror. The difference in height between the plane mirror and micro-mirror causes the OPD between the two beams reaching the detector to be different, thereby forming interference fringes on the detector. Therefore, image and spectral information regarding the target reaches the detector. Then the scanning mirror rotates, and the target is imaged on the next step surface, so the detector can obtain interference information concerning different OPDs of the target. After one scan period, the detector obtains a three-dimensional data cube containing two-dimensional spatial information and one-dimensional spectral information.

Optics EXPRESS

2.2. Overall parameters

The instrument uses a medium-wave infrared HgCdTe area array detector, with a response band of 3.7~4.8 μm. The F# is 4. The pixel number is 320 × 256. The pixel size is 30 μm × 30 μm. The theoretical spatial resolution of the instrument is 0.833 m at 2000 m. The theoretical width is 213 m at 2000 m.

2.3. Stepped micro-mirror

Figure 2(a) shows the stepped micro-mirror prototype, with its partial enlargement shown in Fig. 2(b).

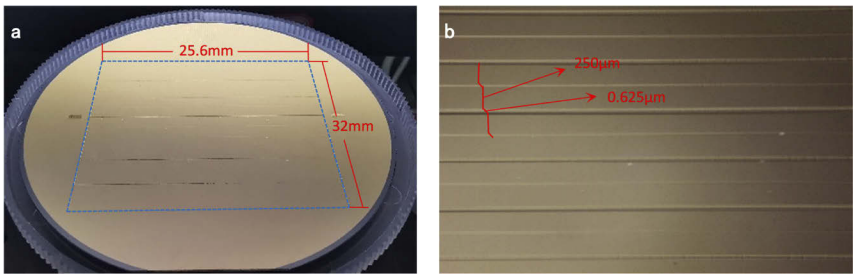

Fig. 2. (a) Prototype of the stepped micro-mirror (steps are all in the dotted line). (b) Partial enlargement of the stepped micro-mirror.

The micro-mirror is made by a micro-nano process, and the design parameters are shown in Table 1.

Table 1. Design parameters of the stepped micro-mirror

Design parameters	Value
Number of steps	128
Total length/mm	25.6
Total height/μm	80
Total width/mm	32
Sub-step height/μm	0.625
width of a sub-step/mm	0.25

The sub-step height design is as follows: Let the optical signal wavelength range be $[\lambda_{min}, \lambda_{max}]$, and the sub-step height of the step micro-mirror be d, then the OPD sampling interval is 2d. According to the Nyquist-Shannon sampling theorem, the sampling frequency should be greater than twice the maximum signal frequency, that is, the sampling interval should satisfy $2d \leq \lambda_{min}/2$, and the sub-step height of the micro-mirror should satisfy $d \leq \lambda_{min}/4$. Substituting λ_{min} into the working band of the instrument, 3.7~4.8 μm, and get $d \leq 3.7/4 = 0.925$ μm. With respect to adjustment-error influence and micro-mirror-processing precision, the OPD during sampling has a certain error, and a certain margin should be left for the sampling interval. Therefore, we set the sub-step height of the micro-mirror to 0.625 μm.

For non-uniformity sampling correction in subsequent data processing, we used a stylus profiler to measure the micro-mirror step height. The probe scanning distance of the stylus profiler was 32 mm, covering all steps from the lowest to the highest. The scanning speed was 100 μm/s and the scanning frequency was 100 Hz. Figure 3(a) shows the sub-step height distribution of the test data; the test data was processed summarized. Figure 3(b) shows the sub-step height distribution histogram, and the measured parameters are summarized in Table 2.

Optics EXPRESS

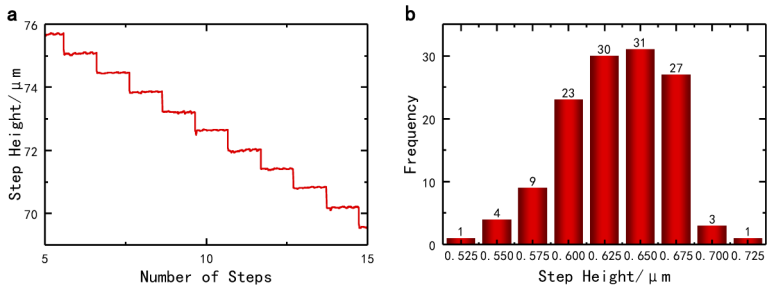

Fig. 3. (a) Partial distribution of the step height. (b) Sub-step height distribution histogram.

Table 2. Measured parameter of the stepped micro-mirror

Measured parameter	Value
Average sub-step height/μm	0.6189
Standard deviation/μm	0.0348
Surface roughness/μm	0.0192

3. Data processing

The data processing process takes place on the data cube to obtain the scene image and reconstructed spectrum, the flow of which is in Fig. 4. The image is divided into different image units according to the different interference orders. The next processing stage comprises two routes. The first route involves stitching and reconstructing the scene image. We stitch image units of the same order in each image according to scanning direction to obtain the sequence of scene images; we then fuse the images to finally obtain the scene image. The second route involves stitching the interferogram sequence and reconstructing the spectrum. We stitch image units of different orders of the same target in each image according to the OPD sequence, to obtain the target interference pattern sequence, and then perform dimensionality reduction, baseline correction, apodization, non-uniformity sampling correction, and a Fourier transform on the target interferogram sequence to obtain the reconstructed spectrum.

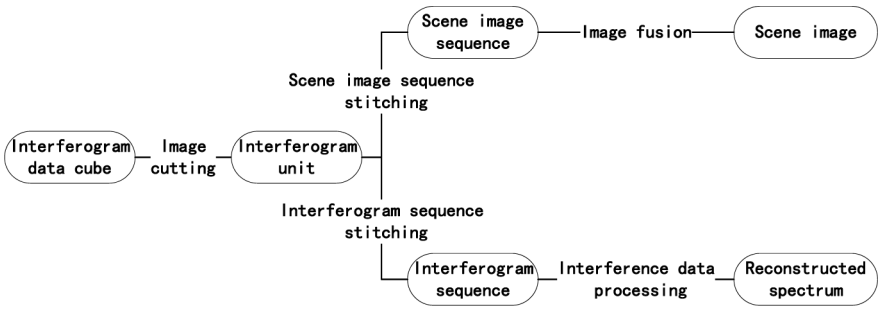

Fig. 4. Data processing flow chart.

3.1. Image cutting

Image cutting forms the basis of subsequent data processing. In theory, the image-unit position corresponding to each interference order is determined by the geometric shape of the stepped micro-mirror. However, the low precision in micro-mirror manufacturing and the instrument

Optics EXPRESS

adjustment error, may cause alignment errors in the optical system; therefore, the image-unit widths corresponding to different interference orders may be different and the Hough transform method is chosen for image-unit separation.

The Hough transform is an effective curve-detection method, converting images from coordinate space to parameter space, detecting curves that can be parameterized, and controlling detection length by setting thresholds, thus filtering out unwanted ones. After detecting the step edge using the Hough transform, and using micro-mirror parameters, interpolation obtains the undetected edge; the least-squares method fits the corresponding line—the edge of the interference image unit.

3.2. Image stitching

Due to the difference in the widths between the different sub-steps of the micro-mirror, if the interferogram units are simply combined in order, the resulting stitched image has a stitching gap. Therefore, we use feature-based image-stitching methods to stitch scene images, the main steps of which include feature extraction, image registration, and image fusion.

The first step is feature extraction, where the considerably robust scale invariant feature transform (SIFT) algorithm is used [19,20]. The SIFT algorithm must usually be divided into several steps: detecting and locating scale-space extreme points, determining feature-point directions, and generating feature descriptors. We only use the algorithm to determine extreme-point position. To detect stable extreme points in scale space, we adopt Gaussian difference scale space, using different scale Gaussian difference kernels for convolution generation of images:

$$D(x, y, \sigma) = (G(x, y, k\sigma) - G(x, y, \sigma)) \otimes I(x, y) = L(x, y, k\sigma) - L(x, y, \sigma) \tag{1}$$

where $G(x, y, \sigma) = \exp(-(x^2 + y^2)/2\sigma^2)/2\pi\sigma^2$, and $G(x, y, \sigma)$ is a Gaussian function of varying scale; (x, y) and σ are the space and scale coordinates, respectively.

The second step is image registration. We use the feature matching algorithm based on local maximum entropy to obtain the matching result with greatest credibility, via correlation matching of local feature points. Entropy [21] expresses the complexity or uncertainty of a system, and can be used to describe mutual information, representing the statistical correlation between two random variables. Image matching based on mutual information searches for the pair of points with the largest amount of mutual information among the two images to be registered, obtaining the feature-point matching pair of the image. For an m × n image module, entropy is:

$$H_f = -\sum_{i=1}^{m}\sum_{j=1}^{n} p_{ij} \log p_{ij} \tag{2}$$

where p_{ij} represents the grayscale distribution of the image in (i, j) coordinates. If $H(A)$, $H(B)$ represent the entropy of images A and B, respectively, and $H(A, B)$ represents the joint entropy of the two images, then the information amount is:

$$K(A, B) = H(A) + H(B) - H(A, B) \tag{3}$$

The third step is image fusion. The stitched image has a number of vertical stitching gaps, periodically arranged. After a two-dimensional fast Fourier transform, the vertical stitching gap in the image peaks on the horizontal axis of the Fourier frequency domain energy spectrum. Therefore, we can choose the appropriate filter and multiply it with the previously obtained frequency domain energy distribution, so that the gap components in the frequency domain space can be filtered out. Finally, we perform an inverse Fourier transform on the filtered spectrum to obtain a spatial image without stitching gaps.

Optics EXPRESS

3.3. Spectral reconstruction

Using the above stitching method, we stitch image units of different orders of the same target in each image according to the OPD sequence. The interferogram sequence of the target is thus obtained, meaning the spectrum can now be reconstructed. Due to the instrument's structure, our spectral reconstruction method consists of: (1) dimensionality reduction, (2) baseline correction, (3) apodization, and (4) Fourier transform.

(1) The dimensionality reduction of the interferogram sequence is represented by the following two equations:

$$I_0 = \begin{bmatrix} I_{11} & \cdots & I_{1n} \\ I_{21} & \cdots & I_{2n} \\ \vdots & \cdots & \vdots \\ I_{m1} & \cdots & I_{mn} \end{bmatrix} \begin{matrix} I_{1(n+1)} & \cdots & I_{1(n\times N)} \\ I_{2(n+1)} & \cdots & I_{2(n\times N)} \\ \vdots & \cdots & \vdots \\ I_{m(n+1)} & \cdots & I_{m(n\times N)} \end{matrix} \tag{4}$$

$$I_0' = (I_1' I_2' I_3' I_4' \cdots I_N') \tag{5}$$

Equation (4) represents a two-dimensional interferogram sequence, the matrix in the box represents an image in a sub-step mirror, and N represents the number of sample points resampled. Equation (5) represents a one-dimensional interference intensity sequence after dimensionality reduction.

(2) In baseline correction, the interference intensity sequence consists of two parts, the DC-component and the AC-component. Due to the linearity of the Fourier transform, the AC-component modulates the interferogram, determining the shape and peak position of the spectrum, but the DC-component has little effect. When error exists in the DC-component, it causes a baseline curvature of the interference intensity sequence. The least-squares method is used to fit the baseline of the interference intensity sequence, and then obtain the corresponding DC-components at different sampling points. Finally, the corresponding DC-component value is subtracted from the intensity value of each sampling point in the interference intensity sequence.

(3) In apodization, the integral interval of the Fourier transform is infinite, but acquisition of the interferogram can only be performed in a limited interval, called the "sampling cutoff." Sampling cutoff causes side-lobe oscillation in the spectrum, and the first side-lobe should be no more than 22% larger than the main peak. Therefore, the apodization function must apodize the interference intensity sequence to mitigate side-lobe oscillation. We use the Happ-Genzel function, which has little influence on spectral resolution. Let the sampling length be Δ:

$$A(\delta) = 0.54 + 0.46 \cos\left(\pi\left(\frac{2\delta}{\Delta} + 1\right)\right) \tag{6}$$

(4) We perform a fast Fourier transform on the interference intensity sequence to obtain the reconstructed spectrum.

3.4. Non-uniformity sampling correction

Due to the influence of the substrate material and manufacturing process, the height of each sub-step of the micro-mirror can be offset from the theoretical height, so the errors will be introduced into the OPD corresponding to each interference order. Set the height of the sub-step of the stepped micro-mirror to $\delta/2$ and the sampling point to N. Therefore, the sampling interval is 2δ and the maximum OPD of the instrument is $N\delta$. According to Fourier transform infrared

Optics EXPRESS

spectroscopy [22], for the *n-th* ($n = 0, 1, \ldots, N-1$) sampling point in the frequency domain, the wavenumber is $\nu_{n0} = 1/(N\delta)$. Set OPD errors to $\varepsilon_i (i = 1, 2, \ldots, N)$, the sampling interval in the frequency domain will turn into $\nu_n = 1/(N\delta + \sum_{i=1}^{N} \varepsilon_i)$. Its spectral intensity has the following relationship with the interference intensity in the OPD domain:

$$\begin{cases} B(\nu_n) = \int_{-\infty}^{+\infty} I(\delta) \exp(-j2\pi\nu_n\delta) d\delta \\ I(\delta_k) = \int_{-\infty}^{+\infty} B(\nu) \exp(j2\pi\nu\delta_k) d\nu \end{cases} \tag{7}$$

where $k = 0, 1, \ldots, N-1$. Then the phase angle of the *n-th* sampling point is:

$$\theta_{nk} = 2\pi\upsilon_n\delta_k = 2\pi \frac{n}{N\delta + \sum_{i=1}^{N} \varepsilon_i} (k\delta + \varepsilon_k) \tag{8}$$

Therefore, the phase error of the *n-th* sampling point is:

$$\Delta\theta_{nk} = \theta_{nk} - \theta_{nk0} = 2\pi(\nu_n\delta_k - \nu_{n0}\delta_{k0}) = 2n\pi\left(\frac{k\delta + \varepsilon_k}{N\delta + \sum_{i=1}^{N} \varepsilon_i} - \frac{k}{N}\right) \tag{9}$$

The phase error will cause the spectral peaks to shift from the theoretical value.

To correct the above phase error, we performed non-uniformity sampling correction as follows: First, set the height error of the *i-th* sub-step of the micro-mirror as $\varepsilon_i/2$, and the OPD error is ε_i according to the interference principle. Then let $\Delta R_i (i = 1, 2, \ldots, N)$ represent the actual OPD matrix, ΔE_i the OPD error matrix, and ΔI_i the ideal OPD matrix, so that the non-uniformity sampling error correction process is:

(1) Calculate the corresponding height error $\varepsilon_i/2$ based on the measured step-mirror height data (Section 2.3), and calculate the OPD error matrix as $\Delta E_i = \varepsilon_i$; then the actual OPD matrix is:

$$\Delta R_i = \Delta I_i - \Delta E_i \tag{10}$$

(2) Use the least-squares method to fit the functional relationship between the actual OPD matrix and the value of the interference intensity sequence:

$$IR_i = f(\Delta R_i) \tag{11}$$

(3) Substitute the ideal OPD matrix into Eq. (11) to find the ideal interference intensity sequence:

$$II_i = f(\Delta I_i) \tag{12}$$

3.5. Spectral resolution enhancement

Due to the image noise and apodization algorithms, the resolution of the reconstructed spectrum is lower than the theoretical value. Therefore, after analyzing the spectral characteristics, we propose a spectral resolution enhancement algorithm based on empirical mode decomposition (EMD).

EMD is a signal decomposition method proposed by NASA's Huang *et al.*, which decomposes signals into different eigenmode functions according to frequency [23,24]. The eigenmode function must satisfy the following two conditions:

Optics EXPRESS

(1) The number of times the signal passes through the zero point is equal to the number of poles, and if not equal, it is at most one.

(2) The signal is locally symmetrical about the time axis, i.e., the mean value of the upper and lower envelopes at any point on the signal curve is zero.

With the above restrictions, we can decompose the spectral signal, set a spectral signal to $S(f)$, find all the extreme values of $S(f)$, find the upper and lower envelopes by interpolation, and then solve the mean of the upper and lower envelopes $EM_1(f)$; calculate:

$$IMF_1 = S(f) - EM_1(f) \tag{13}$$

If IMF_1 satisfies the constraint condition of the eigenmode function, it is the first eigenmode function, otherwise let $S(f) = IMF_1$; repeat Eq. (13) until IMF_1 satisfies the constraint condition of the eigenmode function. Next, we subtract IMF_1 from the original signal, and take the obtained $S_1(f)$ as the new original signal, obtaining IMF_2 by the above steps. Repeat the above steps to obtain the empirical modal function $IMF_3, IMF_4, \ldots, IMF_{\mathrm{n}}$ until the *n-th* time $S_n(f)$ is a monotonic function, and the eigenmodes satisfying the condition can no longer be obtained. Express the spectral signal in the form of a sum of the empirical modal functions:

$$S(f) = \sum_{i=1}^{n} \omega_i IMF_i(f) + S_n(f) \tag{14}$$

where ω_i is the weight coefficient. Since most of the information in the spectral signal is in the characteristic peak, to enhance spectral resolution, the higher the weight of the high-frequency part of the spectral signal, the higher the spectral resolution. Therefore, an exponential function is used to calculate the weight coefficient: let the maximum value of each eigenmode function be M_i, the initial weight coefficient ω_i, and the new weight coefficient $\omega_i'(i = 1, 2, \ldots, n)$. The new weight coefficients can be calculated by Eqs. (15) and (16):

$$S = \sum_{i=1}^{n} M_i \tag{15}$$

$$\omega_i' = \begin{cases} \omega_1 + \Delta & i = 1 \\ \frac{\omega_i}{e^i} & i = 2, 3, \ldots, n \end{cases} \tag{16}$$

where $\omega_i = M_i/S$, $\Delta = \sum_{i=2}^{n}(\omega_i - \omega_i')$. After obtaining the new weight coefficient, we can reconstruct the spectrum using Eq. (14).

4. Experimental results

The experimental location of this paper is 43° 50' 53.76'' north latitude, 125° 23' 54.96'' east longitude, and the target distance is 725 meters. To obtain the complete data cube of the target, the instrument must accumulate over a certain period of time to make the target traversing all interference orders via swing of the scanning mirror.

4.1. Data acquisition

To obtain the target interferogram from the zero OPD position to the maximum OPD position, the distance that the target moves on the micro-mirror should be less than or equal to the width of one sub-step mirror. To reduce scan time, the distance is set equal to the width of one sub-step mirror. According to the parameters of the first imaging system and the stepped micro-mirror,

Optics EXPRESS

the scanning interval is calculated to be 0.024°. Then, we determine a scan direction and acquire an image after each scan interval of the scan mirror. After one cycle, we obtain a complete interference data cube, shown in Fig. 5.

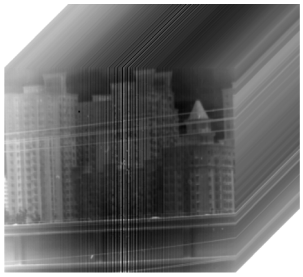

Fig. 5. Interference data cube.

4.2. Experimental results

After obtaining the target's interference data cube, we reconstruct the scene image. Using the method in Section 3.1, we perform a Hough transform and interpolation fitting on the interferogram to obtain the interferogram units, and the results are shown in Fig. 6(a). Then we use the method in Section 3.2 to stitch and fuse the interferogram units. The result of feature-based image stitching is shown in Fig. 6(b), and the result of image fusion is shown in Fig. 6(c).

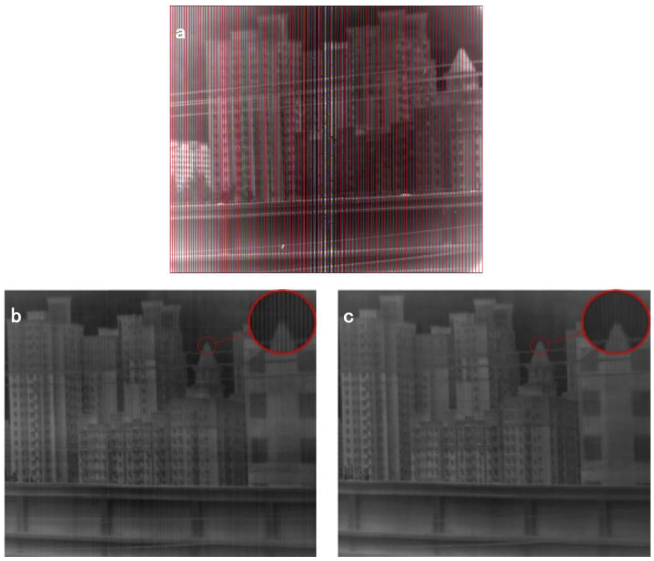

Fig. 6. (a) Interferogram after Hough transform detection and interpolation. (b) Scene image after feature-based image stitching. (c) Scene image after image fusion.

Figures 6(a) and 6(b) show that the stitched image units match very accurately, and the image details in the red circle in Figs. 6(b) and 6(c) show that the stitching gaps and the transition between image units are greatly improved. Our method, therefore, is suitable for scene-image reconstruction of the instrument.

Optics EXPRESS

Next, we reconstruct the spectrum. We select a point in the scene as the target of spectral reconstruction (as shown in Fig. 7(a), select point A as the reconstructed target), then extract and stitch the image units of all orders in the order according to the OPD to obtain a two-dimensional interferogram sequence, as shown in Fig. 7(b).

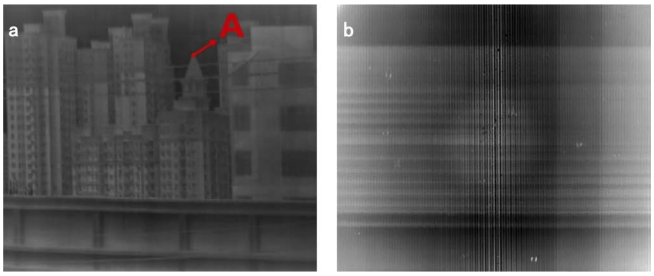

Fig. 7. (a) Reconstructed target in the scene image. (b) Two-dimensional interferogram sequence of the reconstructed target.

We then use the methods in Sections 3.3, 3.4, and 3.5 to process the two-dimensional interferogram sequence. The result is shown in Figs. 8(a)–8(e).

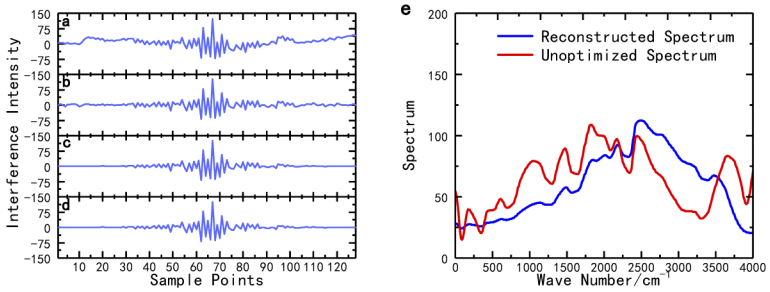

Fig. 8. (a) Interference intensity sequence after dimension reduction. (b) Interference intensity sequence after baseline correction. (c) Interference intensity sequence after apodization. (d) Interference intensity sequence after non-uniform sampling correction. (e) Comparison of unoptimized spectrum and reconstructed spectrum.

After a series of interference data processing, we finally obtain the reconstructed spectrum. Figure 8(e) shows that the optimized spectrum by the above steps has significantly reduced noise and side-lobe oscillation than the unoptimized spectrum, which shows that our method in section 3.3 has obvious effects. It can also be seen from Fig. 8(e) that the peaks of the spectrum before and after the optimization are slightly different, which shows that the non-uniform sampling correction in section 3.4 has a certain improvement on the wavenumber shift of the spectrum.

However, because the composition of the selected spectral reconstructed target is undetermined, and the spectrum is mixed with many unknown atmospheric components, the resulting spectrum cannot evaluate instrument performance in terms of spectral resolution and signal to noise ratio (SNR). Therefore, follow-up experiments are required to evaluate this performance.

5. Instrument performance evaluation

5.1. Spectral resolution

Spectral resolution characterizes the ability of an instrument to resolve adjacent lines. The criterion for distinguishing two adjacent lines of equal intensity and half-height width is that they

Optics EXPRESS

have a depression of not less than 20% of the peak value of the intensity value after synthesis [25,26]. The theoretical calculation formula is:

$$\Delta\upsilon = \frac{1}{\delta_{max}} \tag{17}$$

where $\Delta\upsilon$ is the spectral resolution in cm^{-1} and δ_{max} is the maximum OPD in cm. Substituting $\delta_{max} = 0.625 \times 2 \times 128 \times 10^{-4} = 0.016$ cm, the theoretical spectral resolution is obtained as 62.5 cm^{-1}.

To obtain the true spectral-resolution value, we use the instrument line shape (ILS). The calculation process is as follows: Because of the effect of window truncation caused by limited OPD of the instrument, the actual reconstructed spectrum is:

$$B(\sigma) = FT[\Pi(\delta)I(\delta)]^{-1} = FT[\Pi(\delta)]^{-1} \otimes FT[I(\delta)]^{-1} \tag{18}$$

where $I(\delta)$ is the interference intensity and $\Pi(\delta)$ is the truncation window; i.e., the actual spectrum $B(\sigma)$ can be expressed as the convolution of the ideal spectrum with the Fourier transform of the truncation window. When we only consider the window truncation effect, the ILS is:

$$ILS = FT[\Pi(x)]^{-1} = \int_{-\infty}^{\infty} \Pi(x) e^{-2i\pi\nu x} dx \tag{19}$$

When the ideal spectrum is an infinitely narrow single chromatogram, it is an σ function. According to the nature of the σ function, the actual spectrum is $B(\sigma) = \mathrm{ILS}$; i.e., ILS can be regarded as the output spectrum when the input spectrum is an infinitely narrow single chromatogram, which is determined by the characteristics of the spectrometer and the spectral transformation method [27,28].

According to the above calculation, we design the following ILS measurement experiment: A point-source black body and a narrow-band filter, with a center wavelength of 4.26 μm and a bandwidth of 66cm^{-1}, form a light source, and three calcium fluoride lenses form a collimation system to simulate a collimated monochromatic light source with parallel incidence. The optical path design and experimental platform are shown in Fig. 9(a). Then, we process the experimentally measured data [Fig. 9(b)] to obtain an interference intensity sequence [Figs. 9(c) and 9(d)], obtaining ILS as shown in Fig. 9(e).

Figure 9(e) shows that the main peak position of the ILS without non-uniformity sampling correction is 2398cm^{-1}, and the deviation from the theoretical value of 2347.4cm^{-1} is 1.28%. After non-uniformity sampling correction, the ILS main peak position is 2364cm^{-1}, only 0.41% from the theoretical value, 2347.4cm^{-1}, indicating that non-uniformity sampling correction effectively corrects the wavenumber shift of the spectrum caused by the step-height shift. However, the half-width (spectral resolution) is 79cm^{-1}, quite different from the instrument index, 62.5cm^{-1}. This is probably because of the narrow band source that replaces the monochromatic source, leading to ILS broadening. Therefore, we further processed the interference data, to enhance the resolution of ILS to bring it closer to the theoretical value. After spectral resolution enhancement, the ILS spectral resolution reached 65cm^{-1}, very close to the theoretical value of 62.5cm^{-1}.

5.2. Signal to noise ratio

The signal to noise ratio (SNR) is also an important performance characterization parameter of the spectrometer, related to factors such as target radiation and reflection characteristics, background characteristics, atmospheric transmittance, optical system aperture, relative aperture, transmittance, detector responsiveness, quantum efficiency, and specific detection rate [29,30]. Because the final data obtained by the instrument includes both interference images and spectral information, the SNR of the interferogram and the SNR of the reconstructed spectrum must be

Optics EXPRESS

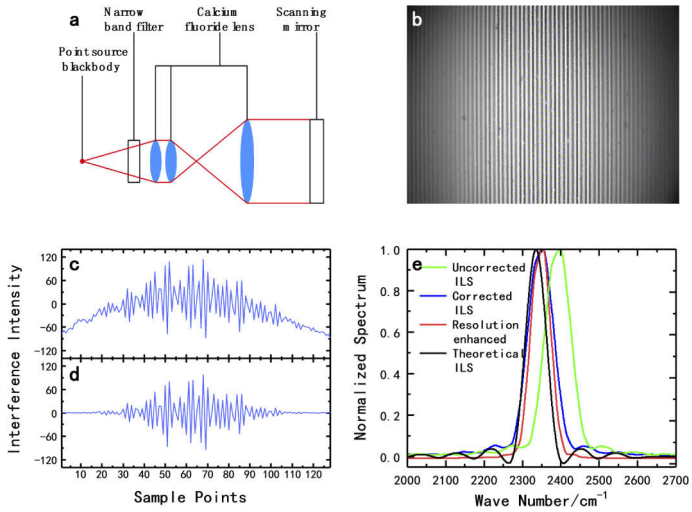

Fig. 9. (a) Simplified configuration of the ILS measurement system. (b) Two-dimensional interferogram sequence. (c) Interference intensity sequence. (d) Interference intensity sequence after data processing. (e) Instrument line shape.

measured simultaneously, where the interferogram SNR reflects original-image quality, and the reconstructed-spectrum SNR reflects the instrument's spectral response performance.

First we calculate the theoretical SNR value. The theoretical value of the interferogram SNR is derived as follows: Set the detector area toA_d, the focal length of the optical system to f, the incident aperture to$D$, the atmospheric transmittance to τ_a, the optical system transmittance to τ_0; the target spectral radiance is L_λ. The luminous flux to the detector is:

$$\phi_{\lambda d} = \frac{\pi A_d L_\lambda \tau_a D^2(\lambda)\tau_0(\lambda)}{4f^2} \tag{20}$$

The corresponding output signal voltage of the detector is:

$$V(\lambda) = \phi_{\lambda d} R(\lambda) = \frac{\pi A_d L_\lambda \tau_a D^2(\lambda)\tau_0(\lambda)R(\lambda)}{4f^2} = \frac{\pi A_d L_\lambda \tau_a D^2(\lambda)\tau_0(\lambda)V_s D^*}{4f^2(A_d\Delta f)^{1/2}} \tag{21}$$

where $R(\lambda)$ is the spectral response rate of the detector, V_s is the total output noise, D^* is the spectral ratio detection rate, $\Delta f = 1/2t_{\text{int}}$ is the noise equivalent bandwidth, and t_{int} is the detector integration time. Then, the SNR (integral form) is:

$$SNR_x = \frac{V(\lambda)}{V_s} = \frac{\pi D^2\sqrt{A_d}}{4f^2\sqrt{\Delta f}} L_\lambda \tau_a(\lambda)\tau_0(\lambda)D^*(\lambda)d\lambda \tag{22}$$

Rewrite Eq. (22) by use the average over the wavelength range:

$$SNR_x = \frac{\pi D^2\sqrt{A_d}}{4f^2\sqrt{\Delta f}} L\tau_a\tau_0 D^*\Delta\lambda \tag{23}$$

where $L = \varepsilon W/\pi = \varepsilon c_1/(\pi\lambda^5 \times (e^{c_2/\lambda T} - 1))$ is the target spectral radiance, ε is the emissivity, W is the spectral radiant flux density, $c_1 = 3.7415 \times 10^{-16} W \cdot m^2$ is the first radiation constant, $c_2 = 1.43879 \times 10^{-2} m \cdot K$ is the second radiation constant, and T is the absolute temperature of

Optics EXPRESS

the target. Substituting various parameters into Eq. (23), set the target temperature to $T = 700\ K$ and calculate the theoretical value of the SNR of the interferogram: $SNR_x = 204.4829$.

The theoretical SNR value of the reconstructed spectrum is derived as follows [31]: The Fourier transform relationship between interference intensity $I(x)$ and spectral intensity $B(\sigma)$ is:

$$\begin{cases} B(\sigma) = \int_{-\infty}^{+\infty} I(x) \exp(-i2\pi\sigma x) dx \\ I(x) = \int_{-\infty}^{+\infty} B(\sigma) \exp(-i2\pi\sigma x) d\sigma \end{cases} \tag{24}$$

According to the Paseval theorem [32]:

$$\delta\upsilon \overline{|B|}^2 = \delta x \overline{|I|}^2 \tag{25}$$

where $\delta\upsilon$ is the spectral resolution and δx is the OPD sampling interval. For this instrument, the following relationship exists:

$$\begin{cases} \delta x = 2\delta / N \\ \delta\upsilon = 2\upsilon_{max} / N \\ N \times \delta x \times \delta\upsilon = 1 \end{cases} \tag{26}$$

where N is the number of bilateral sampling points, υ_{max} is the maximum wave number difference, and $-\delta \sim \delta$ is the OPD sampling range. Multiply both sides by the number of bilateral sampling points to get:

$$2\upsilon_{max} \overline{|B|}^2 = 2\delta \overline{|I|}^2 \tag{27}$$

giving the conversion relationship between frequency-domain noise and airspace noise as:

$$\varepsilon_\sigma = \varepsilon_x \sqrt{\delta / \upsilon_{max}} = \frac{\delta\sigma N \overline{B(\sigma)}}{\sqrt{2} SNR_x} \sqrt{\delta / \upsilon_{max}} \tag{28}$$

where $\overline{B(\sigma)}$ is the average of the spectral intensities at N sampling points. Then, the spectrum's SNR is:

$$SNR_\sigma = \frac{\overline{B(\sigma)}}{\varepsilon_\sigma} = \sqrt{\frac{2}{N}} SNR_x \tag{29}$$

Substituting $N = 128$, $SNR_x = 204.4829$ into Eq. (29); the SNR theoretical value of the reconstructed spectrum is $SNR_\sigma = 25.5604$.

Measure and calculate the SNR true value, where measurement of the SNR true value of the interferogram is as follows: Choose the SNR at the 0-path difference with the largest interference intensity as the SNR of the interferogram:

$$SNR_x = \frac{\overline{I_0}}{\sigma[I_0]} \tag{30}$$

where I_0 represents the interference intensity at the 0-path difference.

Use the point source black body and the integrating sphere to simulate an approximately uniform surface light source; set the temperature to be the same as the theoretical calculation, then use the instrument to scan one cycle to obtain a time-dimensional 0-path difference interference intensity sequence. Calculate the mean and standard deviation of the sequence and substitute them into Eq. (30) to obtain the interferogram SNR.

Measure the true value of the reconstructed spectrum's SNR as follows: Use the data obtained from the interferogram-SNR calculation to obtain the black body's reconstructed spectrum;

Optics EXPRESS

compare it with the theoretical (simulated) black body spectrum; substituting the data into the following formula, the spectrum's average SNR is:

$$SNR_\sigma = \sum_{i=1}^{n} SNR_\sigma(i) = \sum_{i=1}^{n} \frac{B(i)}{\sigma(i)} \tag{31}$$

where n is the number of spectral channels, $SNR_\sigma(i)$ is the SNR of the i-th spectral channel, $B(i)$ is the reconstructed spectrum of the i-th spectral channel, and $\sigma(i)$ is the noise standard deviation of the i-th spectral channel. Figure 10 is the measured blackbody interference data, and the comparison between the reconstructed spectrum post-processing and the blackbody theoretical spectrum.

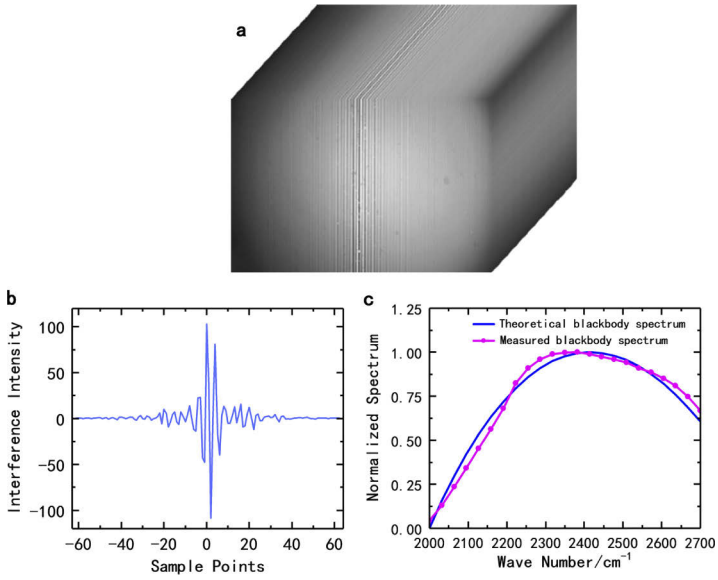

Fig. 10. (a) Interference data cube of blackbody. (b) Interference intensity sequence of blackbody. (c) Theoretical spectrum and reconstructed spectrum of blackbody.

It can be seen from Fig. 10(c) that the theoretical spectrum and the measured spectrum of blackbody are slightly different. This is due to the influence of some factors, such as the interference of the experimental environment, the non-uniform spectral response of the detector and the uneven transmittance of the anti-reflection coated lens during the spectral response range.

After calculation, the measured value of the interferogram SNR is: $SNR_{xt} = 189.3201$, and the measured value of the reconstructed-spectrum SNR is: $SNR_{\sigma t} = 22.8817$. Therefore, the interferogram SNR error is 7.42%, and the reconstructed-spectrum SNR error is 10.48%.

6. Conclusions

Several novel algorithms are used to process data related to the characteristics of a stepped micro-mirror to eliminate the image's stitching gaps, and the spectral noise and side-lobe oscillations to generate a high-quality reconstructed image and an impressive reconstructed target spectrum.

Moreover, to evaluate instrument performance and verify the validity of non-uniformity sampling correction and spectral resolution enhancement, the theoretical values of spectral resolution and the SNR are rigorously derived from the instrument parameters and characteristics. This derivation establish the conversion relationship between the interferogram SNR and the

Optics EXPRESS

reconstructed-spectrum SNR. Experimental results shows that the main peak positions of the ILS before and after non-uniformity sampling correction are 2398cm^{-1} and 2364cm^{-1}, differing by 1.28% and 0.41% from the theoretical value of 2347.4cm^{-1}, indicating that non-uniformity sampling correction does correct wavenumber shift. The spectral resolutions before and after spectral-resolution enhancement are 79cm^{-1} and 65cm^{-1}, differing by 26.4% and 4% from the theoretical value, 62.5cm^{-1}, indicating that the spectral resolution enhancement based on EMD enhances spectral resolution. The interferogram SNR of the instrument is 189.3201 and its error from the theoretical value of 204.4829 is 7.42%. The reconstructed-spectrum SNR of the instrument is 22.8817 and its error from the theoretical value of 25.5604 is 10.48%. Further research will focus on data-processing optimization to improve the accuracy of the main-peak position of the reconstructed spectrum and bring the SNR closer to the theoretical value, thus enhancing the applicability of the instrument.

Funding

National Natural Science Foundation of China (61575193, 61627819, 61727818, 61805239); Jilin Scientific and Technological Development Program (20150520101JH, 20180201024GX, 20190303063SF); Youth Innovation Promotion Association of the Chinese Academy of Sciences (2018254).

Disclosures

The authors declare no conflicts of interest.

References

1. V. Saptari, *Fourier transform spectroscopy instrumentation engineering* (SPIE Press, 2004), Chap. 1.
2. S. Wang and B. Xiangli, "Research of spectrum signal-to-noise ratio of large aperture static imaging spectrometer," Spectrosc. Spect. Anal. **34**(3), 851–856 (2014).
3. P. G. Lucey, M. Wood, S. T. Crites, and J. Akagi, "A LWIR hyperspectral imager using a Sagnac interferometer and cooled HgCdTe detector array," Proc. SPIE **8390**, 83900Q (2012).
4. N. Matallah, H. Sauer, F. Goudail, J. C. Fontanella, Y. Ferrec, J. Taboury, and P. Chavel, "Design and first results of a Fourier Transform imaging spectrometer in the 3–5 μm range," Proc. SPIE **8167**, 816715 (2011).
5. L. V. Egorova and A. S. Anufriev, "An imaging dynamic shearing Fourier spectrometer," J. Opt. Technol. **80**(11), 703–705 (2013).
6. L. Pei, H. Min, Q. Lv, J. Wang, and W. Li, "Optical system design of snapshot imaging spectrometer using image replication based on Wollaston prism," Proc. SPIE **9444**, 94440Y (2015).
7. M. W. Kudenov and E. L. Dereniak, "Compact real-time birefringent imaging spectrometer," Opt. Express **20**(16), 17973–17986 (2012).
8. Y. Chen, D. Xu, K. Xu, N. Zhang, S. Liu, J. Zhao, Q. Luo, L. W. Snyman, and J. W. Swart, "Optoelectronic properties analysis of silicon light-emitting diode monolithically integrated in standard CMOS IC," Chin. Phys. B **28**(10), 107801 (2019).
9. B. Shen, P. Wang, R. Polson, and R. Menon, "An integrated-nanophotonics polarization beamsplitter with 2.4× 2.4 μm 2 footprint," Nat. Photonics **9**(6), 378–382 (2015).
10. D. Dai, J. Bauters, and J. E. Bowers, "Passive technologies for future large-scale photonic integrated circuits on silicon: polarization handling, light non-reciprocity and loss reduction," Light: Sci. Appl. **1**(3), e1 (2012).
11. M. Wang, R. Salut, H. Lu, M. A. Suarez, N. Martin, and T. Grosjean, "Subwavelength polarization optics via individual and coupled helical traveling-wave nanoantennas," Light: Sci. Appl. **8**(1), 76 (2019).
12. X. Jian, C. Zhang, L. Zhang, and B. Zhao, "The data processing of the temporarily and spatially mixed modulated polarization interference imaging spectrometer," Opt. Express **18**(6), 5674–5680 (2010).
13. C. Zhang and X. Jian, "Wide-spectrum reconstruction method for a birefringence interference imaging spectrometer," Opt. Lett. **35**(3), 366–368 (2010).
14. A. Kleinert, F. Friedl-Vallon, T. Guggenmoser, M. Höpfner, T. Neubert, R. Ribalda, M. K. Sha, J. Ungermann, J. Blank, and A. Ebersoldt, "Level 0 to 1 processing of the imaging Fourier transform spectrometer GLORIA: generation of radiometrically and spectrally calibrated spectra," Atmos. Meas. Tech. **7**(12), 4167–4184 (2014).
15. D. C. Soncco, C. Barbanson, M. Nikolova, A. Almansa, and Y. Ferrec, "Fast and accurate multiplicative decomposition for fringe removal in interferometric images," IEEE Trans. Comput. Imaging **3**(2), 187–201 (2017).
16. C. Zhang, Q. Li, T. Yan, T. Mu, and Y. Wei, "High throughput static channeled interference imaging spectropolarimeter based on a Savart polariscope," Opt. Express **24**(20), 23314–23332 (2016).

Optics EXPRESS

17. Y. Tingyu, Z. Chunmin, Z. Jirui, Q. Naicheng, and T. Cuncun, "High resolution channeled imaging spectropolarimetry based on liquid crystal variable retarder," Opt. Express **26**(8), 10382–10391 (2018).
18. W. Wang, J. Liang, Z. Liang, J. Lü, Y. Qin, C. Tian, and W. Wang, "Design of spatio-temporally modulated static infrared imaging Fourier transform spectrometer," Opt. Lett. **39**(16), 4911–4914 (2014).
19. D. G. Lowe, "Distinctive image features from scale-invariant keypoints," Int. J. Comput. Vis. **60**(2), 91–110 (2004).
20. M. Gong, S. Zhao, L. Jiao, D. Tian, and S. Wang, "A novel coarse-to-fine scheme for automatic image registration based on SIFT and mutual information," IEEE Trans. Geosci. Electron. **52**(7), 4328–4338 (2014).
21. S. F. Gull and J. Skilling, "Maximum entropy method in image processing," in *Proceedings of IEEE Conference on Communications, Radar and Signal Processing*, (IEEE, 1984), pp. 646–659.
22. P. R. Griffiths and J. A. D. de Haseth, *Fourier Transform Infrared Spectrometry* (John Wiley & Sons, 2007), Chap. 4.
23. N. E. Huang, Z. Shen, S. R. Long, M. C. Wu, H. H. Shih, Q. Zheng, N. C. Yen, C. C. Tung, and H. H. Liu, "The empirical mode decomposition and the Hilbert spectrum for nonlinear and non-stationary time series analysis," in *Proceedings of the Royal Society of London. Series A: Mathematical, Physical and Engineering Sciences* (Academic, 1998), pp. 903–995.
24. R. Wenyi, Z. Chunmin, M. Tingkui, F. Lili, and J. Chenling, "Empirical mode decomposition based background removal and de-noising in polarization interference imaging spectrometer: erratum," Opt. Express **21**(8), 10207 (2013).
25. K. Xu, "Monolithically integrated Si gate-controlled light-emitting device: science and properties," J. Opt. **20**(2), 024014 (2018).
26. Y. Bao, X. Yi, Z. Li, Q. Chen, J. Li, X. Fan, and X. Zhang, "A digitally generated ultrafine optical frequency comb for spectral measurements with 0.01-pm resolution and 0.7-μs response time," Light: Sci. Appl. **4**(6), e300 (2015).
27. F. Hase, T. Blumenstock, and C. Paton-Walsh, "Analysis of the instrumental line shape of high-resolution Fourier transform IR spectrometers with gas cell measurements and new retrieval software," Appl. Opt. **38**(15), 3417–3422 (1999).
28. C. Bernardo and D. W. Griffith, "Fourier transform spectrometer instrument lineshape (ILS) retrieval by Fourier deconvolution," J. Quant. Spectrosc. Radiat. Transfer **95**(2), 141–150 (2005).
29. Z. L. Yuan, C. M. Zhang, and B. C. Zhao, "Study of SNR of a novel polarization interference imaging spectrometer," Acta Phys. Sin. **56**(11), 6413–6419 (2007).
30. K. Xu, "Silicon MOS optoelectronic micro-nano structure based on reverse-biased PN junction," Phys. Status Solidi **216**(7), 1800868 (2019).
31. H. Y. Luo, W. Xiong, H. L. Shi, and Z. W. Li, "Study for Signal-to-Noise Ratio of Spatial Heterodyne Spectrometer," Acta Opt. Sin. **37**(6), 0612001 (2017).
32. J. W. Brault and A. Labeyrie, "High resolution in astronomy: Fifteenth Advanced Course of the Swiss Society of Astronomy and Astrophysics," Geneva Observatory **15**, 3–61 (1985).